Satellite-sensor calibration verification with the cloud-shadow method

Phillip N. Reinersman, Kendall L. Carder, and Feng-I R. Chen

An atmospheric-correction method appropriate for high-spatial-resolution sensors that uses cloud-shaded pixels together with pixels in a neighboring region of similar optical properties is described. This cloud-shadow method uses the difference between the total radiance values observed at the sensor for these two regions, thus removing the nearly identical atmospheric radiance contributions to the two signals (e.g., path radiance and Fresnel-reflected skylight). What remains is largely due to solar photons backscattered from beneath the sea to dominate the residual signal. Normalization by the direct solar irradiance reaching the sea surface and correction for some second-order effects provides the remote-sensing reflectance of the ocean at the location of the neighbor region, providing a known ground target spectrum for use in testing the calibration of the sensor.

A similar approach may be useful for land targets if horizontal homogeneity of scene reflectance exists about the shadow. Monte Carlo calculations have been used to correct for adjacency effects and to estimate the differences in the skylight reaching the shadowed and neighbor pixels. © 1998 Optical Society of America

OCIS codes: 010.0010, 010.1320, 010.4450, 120.0280, 280.1310.

1. Introduction

Accurate calibration of aircraft and spaceborne sensors that view dark targets such as the ocean is critical. As much as 90% of the signal at the sensor is due typically to the atmosphere; as little as 10% of the signal may be due to target reflectance.[1,2] Therefore a 5% sensor calibration error may result in an error of as much as 50% in the calculated reflectance. Prelaunch calibration accuracies of 2–5% are representative of requirements for space sensors, and in-orbit sensor performance typically differs from prelaunch performance. Because sensor performance degrades over the life of the mission, occasional recalibration with aircraft- or ground-based methods[3,4] is required.

The method of choice for sensor calibration when viewing the ocean from an aircraft or space is to locate a region with relatively stable and homogeneous optical properties (e.g., the Sargasso Sea), measure its water-leaving radiance spectrum, and determine the optical properties of the atmosphere coincidentally with a sensor overpass.[2,4,5] Then the radiance at the top of the atmosphere can be modeled, and the sensor calibration can be adjusted to produce consistent results. But new calibration strategies will be required for high-spatial-resolution sensors employed in coastal applications where variable bottom reflection and horizontal gradients in water constituents make conventional surface calibration difficult.

In this paper we describe an atmospheric-correction method that uses cloud-shadowed pixels in combination with unshadowed pixels in a neighboring region of similar optical properties. The cloud-shadow method uses the difference in the total radiance reaching the sensor, $L_t(\lambda)$, from these two regions. This allows nearly identical contributions to the two signals (e.g., path radiance and Fresnel-reflected skylight) to be removed, leaving mostly solar photons backscattered from beneath the sea to dominate the residual signal. Normalization by the direct solar irradiance reaching the sea surface provides, to first order, the remote-sensing reflectance of the ocean at the location of the neighbor region. Special attention must be paid to evaluating and correcting for adjacency effects and the difference in skylight reaching the shadowed and neighbor pixels.

The Airborne Visible-InfraRed Imaging Spectrometer (AVIRIS), flying at an altitude of 20 km, provides data simulating that expected from hyperspectral space sensors of the future.[6] Data from the AVIRIS
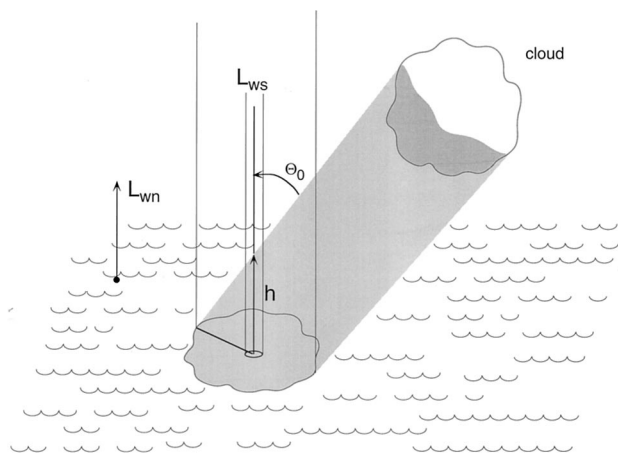
Fig. 1. Geometric demonstration scene of a paired cloud and shadow arrangement.

were used to develop and test the methodology that we describe in this paper.

2. Theoretical Considerations

For illustrative purposes, imagine a viewing situation in which the sensor calibration is correct. The solar zenith angle θ_0 is 45°, and the angle from the pixel to the sensor θ is approximately 0° (see Fig. 1). A small, compact cumulus cloud removes direct solar photons and shadows a region. The water-leaving radiance directed toward the sensor from this shadowed region is designated L_{ws}. (Note that terms indicating wavelength dependence are left out for brevity in cases in which doing so is unlikely to cause confusion.) This radiance results from skylight photons reflected by the surface or scattered from beneath the ocean surface.

Adjacent to the shadowed region is a neighboring patch of water with inherent optical properties identical to those of the shadowed region. This region is illuminated by direct solar photons as well as skylight. The water-leaving radiance from the neighbor region is designated L_{wn}.

In addition to the water-leaving radiance, the sensor measurement includes the effects of path radiance caused by atmospheric scattering of photons into the field of view of the sensor. Path radiance may include solar photons backscattered into the field of view without interacting with the sea surface and forward-scattered photons that have been reflected from the sea surface either before or after scattering. The primary processes responsible for path radiance are molecular (or Rayleigh) scattering and particulate (or aerosol) scattering. Path radiance can be attributed, therefore, to photons that have suffered only Rayleigh scattering, only aerosol scattering, or some combination of both. These three types of path radiance are denoted by L_r, L_a, and L_{ra}, respectively.

Accordingly, let the total radiance measured at the

sensor when viewing a neighboring area in unshadowed water be given by

$$L_{tn} = L_r + L_a + L_{ra} + t_d L_{wn}, \quad (1)$$

where t_d represents the diffuse transmittance of the atmosphere for water-leaving radiance.[7]

The radiance measured at the sensor when viewing a shadowed pixel can be expressed in the same form, but some differences in the path radiances and diffuse transmittance can be expected. We assume that the cloud is of sufficient thickness that the direct solar beam is completely occluded. Because part of the viewing path to the shadowed pixel is also shadowed, this portion of the viewing path must produce less path radiance (Fig. 1).

The apparent path transmittance of the water-leaving radiance from the shadowed pixel may not be equivalent to the term used in Eq. (1). Use of the diffuse transmittance is justified when viewing a large, homogeneous area. In such a case, target radiance that is forward scattered out of the viewing path is balanced by the radiance scattered into it from adjacent areas of the scene. Thus the apparent attenuation of L_{wn} when viewing a large, homogeneous area is due primarily to backscattering and absorption. In the case of the shadowed pixel, the adjacent areas of the scene are generally brighter, and so the apparent transmittance of the viewing path to the shadow will be enhanced by photons reflected from the bright portion of the image and scattered into the field of view of the sensor.

With these ideas in mind, the total radiance at the sensor when viewing a shadowed pixel can be written as

$$L_{ts} = L_r - \Delta L_r + L_a - \Delta L_a + L_{ra} - \Delta L_{ra}$$
$$+ (t_d + \Delta t_d) L_{ws}, \quad (2)$$

where Δ terms express perturbations that are due to nonhomogeneity in the scene illumination.

In general, water-leaving radiance is the result of backscattering of light that has penetrated the air–sea interface and can be expressed as the sum of two parts: one part caused by backscattering of diffuse skylight and the other by backscattering of the direct solar beam. For the neighbor and shadowed pixels, respectively,

$$L_{wn} = {}_{sky}L_{wn} + {}_{sol}L_{wn}, \quad L_{ws} = {}_{sky}L_{ws}, \quad (3)$$

because ${}_{sol}L_{ws} = 0$.

Even though the cloud is small and occludes a similar portion of the sky for both the shadowed and the neighbor pixels, the diffuse irradiances incident on the two pixels are unequal (see Appendix A). The cloud occludes the brightest part of the sky from the shadowed pixel, i.e., the part containing the radiance that is due to near-forward scattering by aerosols. On the other hand, the neighbor pixel is illuminated by the relatively bright side of the cloud. Therefore the diffuse irradiance at the neighbor pixel may be greater than that in the shadow. Under the as-

sumption that the remote-sensing reflectance for sky-light is about the same at the shadow and neighbor pixels, we can write

$$_{sky}L_{wn} = {}_{sky}L_{ws} + {}_{\Delta sky}L_{ws}, \tag{4}$$

so that

$$L_{tn} - L_{ts} = \Delta L_r + \Delta L_a + \Delta L_{ra} + t_d({}_{sol}L_{wn} + {}_{\Delta sky}L_{ws})$$
$$- \Delta t_{d\ sky}L_{ws}. \tag{5}$$

The first three terms on the right hand side of Eq. (5) depend on the length of the shaded portion of the viewing path to the shadow pixels. The height of the intersection of the viewing path with the upper edge of the cylinder of atmosphere shaded by the cloud can be determined from scene geometry. The height of this intersection will be comparable to the radius of the shadow, probably less than 500 m. The thin layer of atmosphere below this intersection would be the source of less than 15% of the Rayleigh scattering. Therefore we assume that the Rayleigh–aerosol correction term ΔL_{ra} is negligible. Then following Gordon et al.[8] for the aerosol and Rayleigh corrections we can write

$$\Delta L_x = [\omega_x \tau_x' F_0'' P_x(\theta, \theta_0)] t_d'/4\pi, \quad x = a, r, \tag{6}$$

where

τ_x' = the optical thickness of the shaded viewing path for process x;

w_x = the single-scattering albedo for process x;

F_0'' = $F_0 \exp[-(\tau - \tau')/\cos(\theta_0)]$, the direct beam incident at the height of the shadow and path intersection;

F_0 = the extraterrestrial solar irradiance;

$P_x(\theta)$ = the scattering phase function for process x;

$P_x(\theta, \theta_0)$ = $\{P_x(\theta_-) + [\rho(\theta) + \rho(\theta_0)]P_x(\theta_+)\}/\cos(\theta)$;

$\cos(\theta_{+-})$ = $+-\cos(\theta_0)\cos(\theta) + \sin(\theta_0)\sin(\theta)\cos(\phi - \phi_0)$;

$\rho(\theta)$ = the Fresnel reflectance for incident angle θ; and

t_d' = $\exp\{-[(\tau_r - \tau_r')/2 + (\tau_{oz} - \tau_{oz}')]/\cos(\theta)\}$, the diffuse transmittance from the shadow and path intersection to the top of the atmosphere.

A term involving $(\tau_a - \tau_a')$ was neglected in the last expression because diffuse transmissivity that is due to aerosols from the top of this layer is approximately unity.[2] The term τ_{oz}' is also negligible, because ozone is generally found above the cloud layer.

The term involving Δt_d in Eq. (2) represents the apparent increase in diffuse transmittance of water-leaving radiance when viewing a shadowed pixel because of the adjacency effect of the brighter surrounding water. The research of Tanre et al.[9] indicates that this term is proportional to the difference in water-leaving radiances from the shadowed and neighbor pixels and is dependent on the geome-
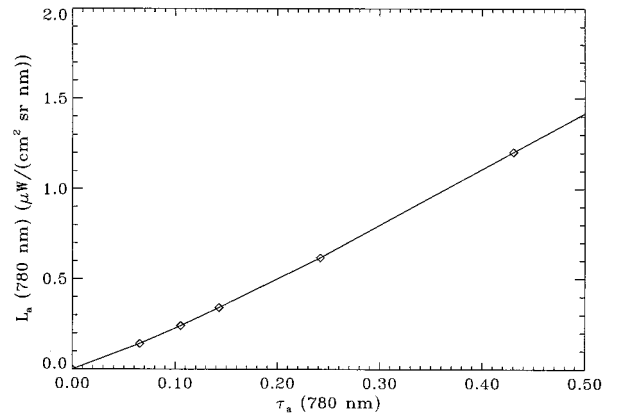

Fig. 2. Scaling relationship between L_a(780 nm) and τ_a(780 nm) derived from LOWTRAN 7.

try of the particular case. Thus, unlike for the $\Delta L_x(\lambda)$ terms, the value of $\Delta t_d(\lambda)$ cannot be determined by use of LOWTRAN 7.[10] Calculating $\Delta t_d(\lambda)$ in the general case would prove difficult and time-consuming, requiring a detailed simulation for each scene used in the sensor calibration. However, in the simplified case of a uniform circular shadow embedded in a brighter, homogeneous background, Δt_d can be expressed in a straightforward manner by use of Eqs. (4)–(6) of Reinersman and Carder.[11] We can write Δt_d as

$$\Delta t_d = t_d \sigma(L_{wn} - L_{ws})/L_{ws} = t_d \sigma({}_{sol}L_{wn} + {}_{\Delta sky}L_{ws})/{}_{sky}L_{ws}, \tag{7}$$

where

$$\sigma = 1 - [t_b + \text{cum}(R)]/t_d. \tag{8}$$

Here t_b is the beam transmittance along the viewing path from the target pixel to the sensor. The cum(R) term represents the apparent increase in path beam transmittance when viewing the shadow center, which results solely from photons that have been reflected from other points in the shadow and subsequently scattered into the field of view of the sensor. Recall that t_d represents the diffuse path transmittance that would be observed if the target pixel were embedded in a uniform background of unshaded water. For a given shadow radius R, Eqs. (18)–(22) of Ref. 11 can be used to estimate cum(R) once the aerosol optical thickness is known.

The approximations in Ref. 11 are based on linear scaling of Elterman's[12] aerosol profiles to match the prevailing atmospheric aerosol optical thickness. To obtain an initial estimate of $\tau_a(\lambda)$, the aerosol optical thickness for wavelength λ, a scaling relationship between τ_a(780 nm) and the aerosol path radiance at 780 nm, L_a(780 nm), was developed by use of LOWTRAN 7 with the U.S. Navy Maritime aerosol model (Fig. 2). This wavelength was chosen to avoid gas absorption bands in the atmosphere and because L_w(780 nm) = 0.0 for nonturbid waters. First, the total radiance reaching the top of the atmosphere,
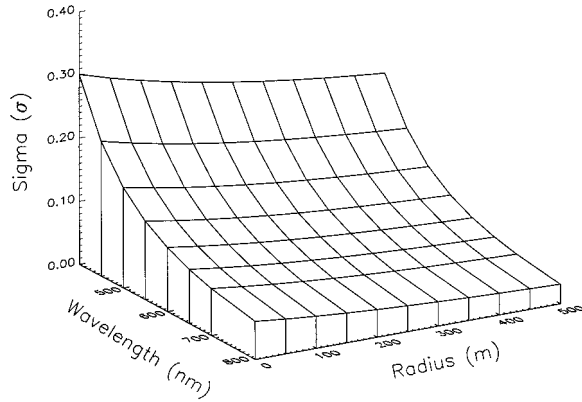
Fig. 3. $\sigma(\lambda, R)$ from backward Monte Carlo simulation.

$L_w(780 \text{ nm})$, was calculated for several values of $\tau_a(780 \text{ nm})$. Then $L_t(780 \text{ nm})$ was calculated for an atmosphere characterized by Rayleigh scattering only. Subtraction of the latter value from the $L_t(780\text{-nm})$ values calculated for the atmospheres containing aerosols yields $L_a(780 \text{ nm})$ because $L_r(780 \text{ nm}) + L_{ra}(780 \text{ nm})$ is approximately constant for $\tau_a(780 \text{ nm}) < 0.5$. Based on the above simulations, we estimate $\tau_a(550 \text{ nm}) = 0.0375$ for the clear conditions encountered when the scenes used in this research were acquired. The behavior of $\sigma(\lambda, R)$ for this aerosol optical thickness is shown in Fig. 3. Thus we estimate that $\sigma(550 \text{ nm})$ is approximately 0.09 for shadows of spherical clouds of the size modeled in this paper when viewed through very clear atmospheres. Fortunately, the algorithm presented subsequently for deducing R_{rs} is relatively insensitive to error in the estimation of Δt_d; a 50% error in the estimation of Δt_d induces only approximately 5% error in the calculated R_{rs}.

Using Eqs. (7) and (5) we obtain

$$(_{sol}L_{wn} + _{\Delta sky}L_{ws}) = (L_{tn} - L_{ts} - \Delta L_a - \Delta L_r)/t_d(1 - \sigma).$$
(9)

we now define

$$\varepsilon(\lambda_i, \lambda_j) = [\omega_a(\lambda_i)\tau_a{}'(\lambda_i)P_a(\theta, \theta_0, \lambda_i)]/$$
$$[\omega_a(\lambda_j)\tau_a{}'(\lambda_j)P_a(\theta, \theta_0, \lambda_j)],$$
(10)

$$S'(\lambda_i, \lambda_j) = \Delta L_a(\lambda_i)/\Delta L_a(\lambda_j)$$
$$= \varepsilon(\lambda_i, \lambda_j)[F_0''(\lambda_i)t_d{}'(\lambda_i)]/[F_0''(\lambda_j)t_d{}'(\lambda_j)].$$
(11)

By use of these results the spectral dependencies in Eq. (9) can be made explicit:

$$t_d(\lambda_i)[1 - \sigma(\lambda_i)][_{sol}L_{wn}(\lambda_i) + _{\Delta sky}L_{ws}(\lambda_i)] = L_{tn}(\lambda_i)$$
$$- L_{ts}(\lambda_i) - \Delta L_r(\lambda_i) - S'(\lambda_i, \lambda_j)\{L_{tn}(\lambda_j) - L_{ts}(\lambda_j)$$
$$- \Delta L_r(\lambda_j) - t_d(\lambda_i)[1 - \sigma(\lambda_i)][_{sol}L_{wn}(\lambda_j) + _{\Delta sky}L_{ws}(\lambda_j)]\}.$$
(12)

If λ_j is a wavelength such as 780 nm where the water-leaving radiance is essentially zero, then $_{sol}L_{wn}(\lambda_j) + _{\Delta sky}L_{ws}(\lambda_j) = 0$, and Eq. (5) becomes

$$\Delta L_a(780 \text{ nm}) = L_{tn}(780 \text{ nm}) - L_{ts}(780 \text{ nm})$$
$$- \Delta L_r(780 \text{ nm}).$$
(13)

This allows Eq. (12) to be rewritten as

$$t_d(\lambda_i)[1 - \sigma(\lambda_i)][_{sol}L_{wn}(\lambda_i) + _{\Delta sky}L_{ws}(\lambda_i)] = L_{tn}(\lambda_i)$$
$$- L_{ts}(\lambda_i) - \Delta L_r(\lambda_i) - S'(\lambda_i, 780 \text{ nm})[L_{tn}(780 \text{ nm})$$
$$- L_{ts}(780 \text{ nm}) - \Delta L_r(780 \text{ nm})].$$
(14)

The cloud height and the height of the shadowed viewing path (h in Fig. 1) can be calculated from scene geometry. Then $\Delta L_r(\lambda)$ can be determined for all λ by subtracting LOWTRAN 7 results for the air column down to height h from the results for the entire air column. The aerosol correction term $\Delta L_a(780 \text{ nm})$ is then determined by Eq. (13). Knowledge of wind speed allows estimation of $\varepsilon(\lambda_i, 780 \text{ nm})$[13] and thus $S'(\lambda_i, 780 \text{ nm})$. $_{\Delta sky}L_{ws}(\lambda_i)$ can be estimated by Monte Carlo simulation (see Appendix A). Thus Eq. (14) allows $_{sol}L_{wn}(\lambda_i)$ to be calculated.

If we assume a Lambertian sky, the average cosine for irradiance at the surface that is due to skylight, $_{sky}E_d(0^+)$, is 0.707.[14] This is roughly equivalent to having all skylight photons striking the sea surface at 45° and is the same as the cosine of the irradiance that is due to direct solar illumination, $_{sol}E_d(0^+)$, in this example. So, because reflectance is independent of the source intensity and color and the illumination geometry is equivalent for the solar and average sky photons in this case,

$$_{sol}R_{rs} = _{sol}L_{wn}/_{sol}E_d(0^+) = L_w/E_d(0^+) = R_{rs}, \quad (15)$$

where R_{rs} is the remote-sensing reflectance that is due to total downwelling irradiance $E_d(0^+)$. Thus deriving R_{rs} in this manner provides a calibrated target reflectance value that can be used to derive the atmospheric aerosol characteristics in a manner similar to that used by Gordon *et al.*[8] for low-chlorophyll, offshore waters.

3. Experiment

We tested the cloud-shadow reflectance method using the AVIRIS data collected from an altitude of 20 km over the Straits of Florida. The AVIRIS produces images consisting of 512 rows of 614 cross-track samples. At each sample location radiance is measured simultaneously in 224 channels. Full coverage of the visible and near-infrared wavelengths is provided with spectral resolution of approximately 10 nm. Spatial resolution for nadir viewing is 20 m.

The scene shown in Fig. 4 is used for the experiment and demonstrations described here. This image was acquired on a SE–NW transect from the Florida Current to Biscayne Bay. Elliot Key is shown in the upper left corner. The shadow neighbor pairs are near the seaward reef edge of Biscayne National Park. The cloud image associated with the
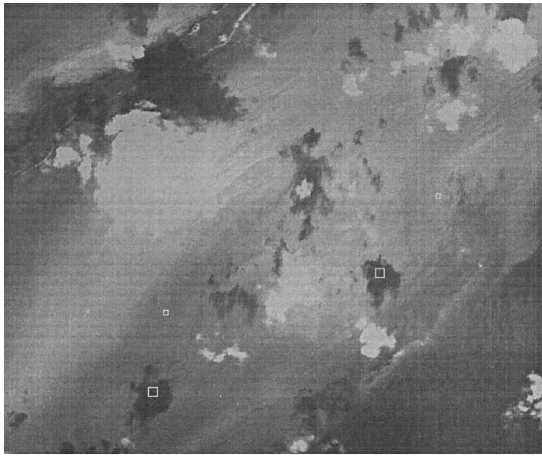
Fig. 4. Locations of sites where the cloud-shadow method was used. Shadow and neighbor regions are marked by boxes.
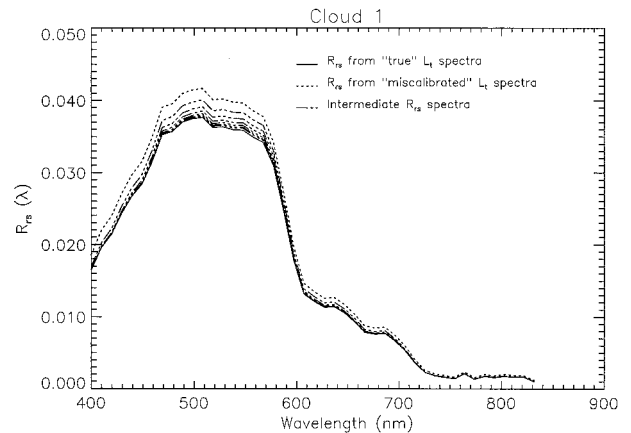

Fig. 5. Illustration of the convergence of the cloud-shadow calibration. Solid curve is the true R_{rs} the dotted curve is R_{rs}' that would be derived if the sensor calibration had been in error by 10%. Intermediate curves indicate the iterative convergence of the cloud-shadow method.

bottom pair (cloud 1) is recorded on the adjoining scene.

Homogeneity of the ocean optical properties around the two cloud-shadow pairs is assumed based on the apparent homogeneity of the scene in those areas. In deep water, away from fronts with sharp gradients in L_w, horizontal homogeneity within a 1-km square is an excellent assumption. For coastal waters, the scene must be scrutinized for gradients in L_w and the shadow and neighbor pairs chosen judiciously. In Fig. 4 it is evident that the assumption of homogeneity is more valid in the neighborhood of cloud 1 and its shadow than that of cloud 2, an issue that may be responsible for the noticeable difference in results from application of the method to the two shadows. Unfortunately, no appropriate clouds were found in nearby scenes of the uniform waters of the Florida Current where the method would be most applicable.

We calibrated the AVIRIS moments before this imagery was collected at a clear-water offshore location in the Florida Current using the vicarious calibration method of Carder *et al*.[5] The calibration area is approximately 25 km southeast of the region shown in Fig. 4. In brief, the R_{rs} curves for calibration scenes are measured, the values of $E_d(0^+)$ are obtained from LOWTRAN 7, and $L_w(\lambda)$ values are calculated by multiplying R_{rs} by $E_d(0^+)$. This technique maintains consistency between the illumination for the atmospheric-correction program and the ocean measurements. The extraterrestrial solar radiance F_0 provided by Neckel and Labs[15] was used as the solar source for all model calculations. Then LOWTRAN 7 was used to calculate the total radiance L_t reaching the sensor from the ocean and the atmosphere. Coincidentally with the R_{rs} measurements, an image of the area was acquired by the AVIRIS. Crests of waves of approximately 100 m in wavelength were observed in the imagery, so the data were median filtered by use of the brightness at 780 nm to discriminate against some 10% of the pixels apparently containing whitecaps and/or Sun glint. Had filtering

not been performed, this enhanced brightness would have been misinterpreted by the program as being part of the atmospheric path radiance. Finally, the calibration of the sensor was adjusted so that modeled and measured L_t values matched. Significant differences relative to preflight calibration values were observed only for wavelengths less than approximately 470 nm.

The first test of the cloud-shadow method was verification that the correct $R_{rs}(\lambda) = L_w(\lambda)/E_d(\lambda)$ spectrum could be recovered from data acquired from an improperly calibrated sensor. $L_t(\lambda)$ spectra from the bottom cloud-shadow pair of Fig. 4 (cloud 1), calibrated as described above, were used to perform the verification. The test procedure was as follows:

(1) The true $L_t(\lambda)$ spectra from both the shadow and the neighbor pixels were increased by 10% to simulate spectra, $L_t'(\lambda)$, that would have been acquired had the sensor calibration been in error by 10%.

(2) $_{sol}L_{wn}'(\lambda)$ was calculated from Eq. (5) as described above by use of $L_t'(\lambda)$. Then the first estimate of the remote-sensing reflectance spectrum $R_{rs}'(\lambda)$ was obtained from

$$R_{rs}'(\lambda) = {}_{sol}L_{wn}'(\lambda)/{}_{sol}E_d(\lambda). \qquad (16)$$

(3) Corrected $L_t'(\lambda)$ spectra at the aircraft were simulated by adding atmospheric effects derived from LOWTRAN 7 for the appropriate conditions, i.e., a nadir-viewing sensor, a 50.8° Sun angle, and a 60-km visibility through a marine aerosol with 80% relative humidity and 1014-mb atmospheric pressure.

The iteration process consisted of repeating steps (2) and (3) above. The results of this method are shown in Fig. 5. Both the true and miscalibrated reflectance spectra are illustrated along with the intermediate results from the cloud-shadow method. After four iterations of recalibration, the corrected
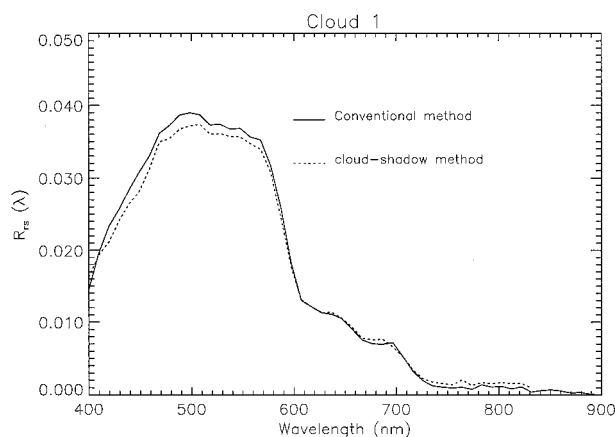
Fig. 6. Remote-sensing reflectance spectra from the bottom site neighborhood of Fig. 2 by use of conventional atmospheric-correction methods and the cloud-shadow method.
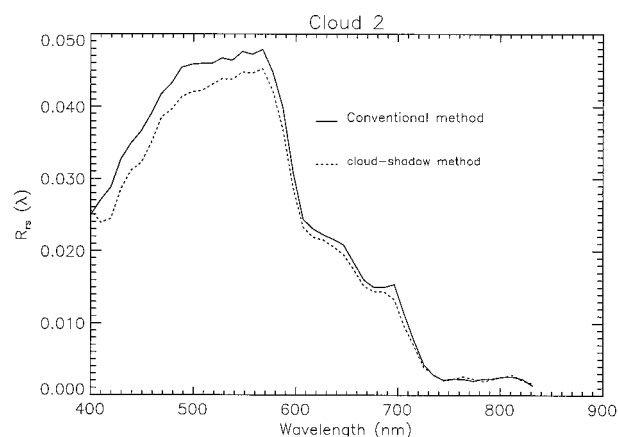

Fig. 7. Remote-sensing reflectance spectra from the top site neighborhood of Fig. 2 by use of conventional atmospheric-correction methods and the cloud-shadow method.

cloud-shadow reflectance spectrum approximates the correct spectrum as closely as if the correct calibration had been used initially.

The method is effective for two reasons: (1) The error in the solar spectrum used to illuminate the atmosphere in the LOWTRAN 7 calculations is less than 2%, and (2) the atmospheric effects simulated by LOWTRAN 7 account for most of the radiance measured by the sensor. $L_t(\lambda)$ can be accurately modeled for clear days because in the visible wavelengths it is dominated by Rayleigh effects that have been accurately quantified. If the sensor calibration were 10% too large, the L_w spectrum calculated conventionally from the difference between L_t and $(L_a + L_r)$ would contain nearly all the error. Thus the conventionally calculated L_w could be 40% or more higher than the true curve. The atmospheric path radiance removed inherently by the cloud-shadow method leaves an estimated L_w spectrum that is high by approximately only 10%, however. Because this spectrum is closer to the correct one, recalibration based on this new ground target reflectance provides a better basis for a second iteration of the recalibration loop, providing a calibration factor that is in error by less than 5%. With iteration, convergence toward a calibration factor consistent with the solar spectrum and the model atmosphere used in LOWTRAN 7 is assured.

4. Results and Discussion

Two further demonstrations of the cloud-shadow atmospheric-correction method were performed by use of the scene shown in Fig. 4.

The results of applying the cloud-shadow method to cloud 1 are compared with conventionally derived results in Fig. 6. Results shown for the conventional method were derived as described in Carder *et al.*[5] with one exception: The water-leaving radiance at 780 nm could not be assumed to be zero, as the method usually requires, because of Sun glint and/or foam effects that are due to the 10–12-m/s winds.[16] Instead, the water-leaving radiance at 780 nm was assumed to equal that determined by the cloud-

shadow method because it inherently separates the atmospheric radiance from all water-leaving radiance including Sun glint and foam effects. The reflectance derived by use of the cloud-shadow method differs from the conventional result by less than 10% from 400 to approximately 460 nm. From 460 to 700 nm, agreement is within approximately 5%.

The results of applying the method to the top shadow neighbor pair (cloud 2) are illustrated in Fig. 7. For this region the cloud-shadow reflectance spectrum is as much as 15% below that for the conventional approach for wavelengths less than 580 nm, whereas for longer wavelengths the comparison is still excellent. Note that the area about the shadow of cloud 2 appears less isotropic than that about the shadow of cloud 1. The discrepancy between the two methods at the shorter wavelengths may be due to differences in bottom depth and/or albedo between the shadow and neighbor pixels. Variability in these bottom characteristics would be masked by attenuation at the highly absorbing, longer wavelengths. But note that for both cloud-shadow regions the conventional method would have seriously overcorrected for aerosol radiance had Sun glint and/or foam effects not been detected and removed by use of the cloud-shadow method.

The discrepancy between the conventionally derived R_{rs} and that resulting from application of the cloud-shadow method for both cloud-shadow pairs appears greatest in the spectral region ranging from approximately 400 to approximately 580 nm. This discrepancy is not likely due to inhomogeneity in atmospheric or marine optical properties. However, the region shown in Fig. 4 is a shallow area where the depth varies from 0 m (at Elliot Key) to approximately 20 m at the southeast corner of the scene, and the bottom is certainly being viewed in large portions of this image. Perturbations in $L_w(\lambda)$ caused by bottom reflectance would be expected in the same spectral region (the most transparent region) as that in which the two methods differ the most.[5] So, although complete analysis of the effect of bottom re-

flectance on the results of the cloud-shadow method has not yet been undertaken, variable bathymetry and bottom albedo are suspected to be the sources of the scene inhomogeneity and of at least part of the inconsistency between the two methods in the spectral range from 400 to 580 nm.

Thus, although the cloud-shadow method cannot provide an atmospheric correction for the entire image (unless the aerosol concentration and type are horizontally homogeneous), it can be used effectively to provide an independent check for specific locations to help identify problems resulting from errors in sensor calibration or atmospheric-correction methodology. For the method to be most useful, horizontal homogeneity in the neighborhood about the cloud and shadow is required.

Appendix A

The term $_{\Delta\text{sky}}L_{ws}(= {}_{\text{sky}}L_{wn} - {}_{\text{sky}}L_{ws})$ that appears in Eq. (14) cannot be derived from LOWTRAN 7. Instead, this quantity was estimated by use of backward Monte Carlo simulation.[11,17,18] The modeled atmosphere consisted of 50 horizontally infinite and homogeneous layers overlying a flat sea surface. Optical properties of the atmosphere were taken from Elterman,[12] with Rayleigh and marine aerosol phase functions as in Reinersman and Carder.[11]

The quantities of interest in these calculations were the differences in downward diffuse irradiances needed to calculate $_{\Delta\text{sky}}L_{ws}$. Photons reflected from the surface of the sea make some contribution to $E_d(0^+)$, as do photons backscattered back into the atmosphere from below the sea surface. But these contributions to $E_d(0^+)$ are probably about the same in the shadow and neighbor regions and would cancel each other in the calculation of $_{\Delta\text{sky}}L_{ws}$. So, for simplicity, the sea surface was modeled as a perfect absorber, and photons that would have impinged on the sea surface more than once were neglected.

Clouds were modeled as spheres that completely displaced the atmosphere in which they were imbedded. The extinction coefficient within clouds was set at 50 km^{-1}, and the single-scattering albedo was set to unity.[19] Scattering within clouds was governed by a single-term Henyey–Greenstein phase function with the asymmetry factor set to 0.85.[20] In the results to follow, cloud 1 and cloud 2 represent the bottom and top cloud-shadow pairs of Fig. 4, respectively. Cloud 1 has a radius of 372 nm and a center height of 942 nm. Cloud 2 has a radius of 350 m and a center height of 1194 m. These parameters were based on estimation of the areas of the shadows and the solar zenith angle of 50.8°.

Photon packets were traced backward from a receiver located on the surface at a point of interest by use of a method derived from Gordon.[18] Each simulation in this research traced 10^5 packets, each initially representing 10^{10} photons, until the weight of the packet was diminished to less than 1 photon. Estimates of the downward diffuse irradiance (normalized by the extraterrestrial solar irradiance) and
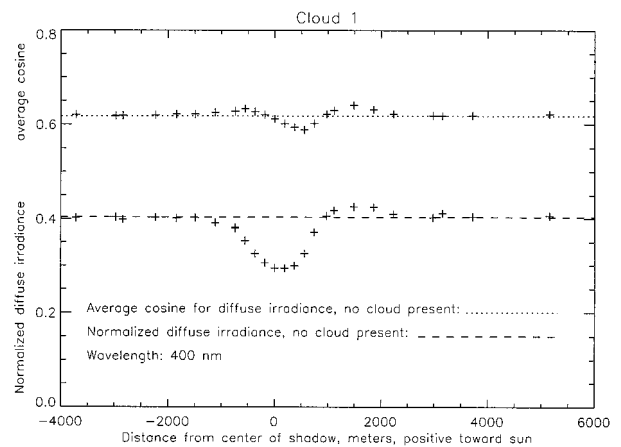

Fig. 8. Normalized downward diffuse irradiance and average cosine for diffuse irradiance in the vicinity of cloud 1 at 400 nm in Elterman's standard atmosphere. Points lie on the surface in the vertical plane containing the Sun, cloud, and shadow center.

the average cosine of the downward diffuse irradiance were acquired for each sensor position modeled.

Preliminary simulations indicated that the diffuse light field is highly variable in the region near and within the shadow. Figures 8 and 9 show the normalized diffuse irradiance and the average cosine for diffuse irradiance at the surface in the vicinity of the Cloud 1 model. These plots represent results modeled at 400 nm with Elterman's standard atmosphere. The points in Fig. 8 are located in the vertical plane containing the Sun, cloud center, and shadow center (SCS plane). The points in Fig. 9 lie on the line perpendicular to the SCS plane through the center of the shadow. Reference lines are included that show the normalized downward diffuse irradiance and average cosine for the same solar zenith angle and atmospheric conditions with no cloud present.
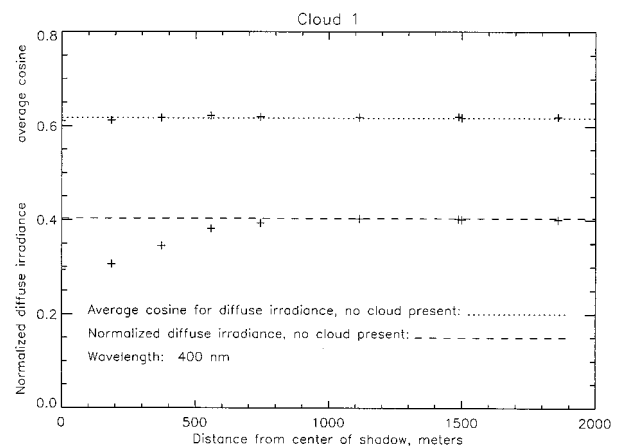

Fig. 9. Normalized downward diffuse irradiance and average cosine for diffuse irradiance in the vicinity of cloud 1 at 400 nm in Elterman's standard atmosphere. Points lie on the surface along a line through the center of the shadow and perpendicular to the vertical plane containing the Sun, cloud, and shadow center.
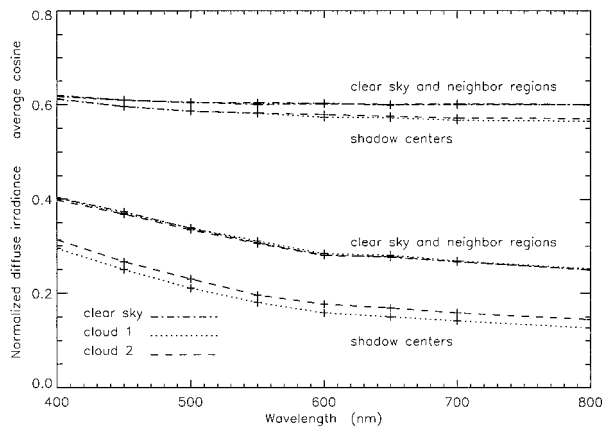
Fig. 10. Normalized downward diffuse irradiance and average cosine at shadow center and neighbor regions for cloud 1 and cloud 2 embedded in Elterman's standard atmosphere. Clear sky values represent conditions with no cloud present.

Fig. 11. Same as Fig. 10, except Elterman's aerosol is scaled so that $\tau_a(550 \text{ nm}) = 0.0375$.

An interesting feature of Fig. 8 is the bright spot appearing directly below and sunward of the cloud. This may be the result of modeling a spherical cloud because, in this case, part of the brightly illuminated side of the cloud is visible from directly below. The features relevant to this research, however, are the depletion of diffuse irradiance at the center of the shadow and the distance to which perturbations that are due to the presence of the cloud extend from the center of the shadow. Many combinations of cloud sizes, cloud heights, and aerosol optical thicknesses were modeled, and the same general features appeared in each case.

Selection of the neighboring region for a cloud shadow involves a compromise. The neighboring region should be near enough to the shadow that the inherent optical properties of the water in both regions are the same, but the neighboring region should be in a location where the downward radiance distribution at the surface is not perturbed by the presence of the cloud. Consider the surface divided into two half-planes by the line through the shadow center and perpendicular to the SCS plane. The results shown in Figs. 8 and 9 indicate that the neighbor region should be located in the half-plane that lies further from the cloud, i.e., on the side of the shadow from which the illuminated face of the cloud is not visible. Neighbor points chosen directly on the SCS plane should be at least 5 cloud radii from the shadow center. Those chosen along the line perpendicular to the SCS plane may be as near as 3 cloud radii to the shadow center.

The data comprising Fig. 10 resulted from modeling cloud 1 and cloud 2 under the same conditions just described. The neighbor region was located in each case 3 cloud radii from the shadow center on the line through the shadow center and perpendicular to the SCS plane. The average cosine of the diffuse irradiance at the neighbor regions is indistinguishable from the clear sky (no cloud present) value. The average cosine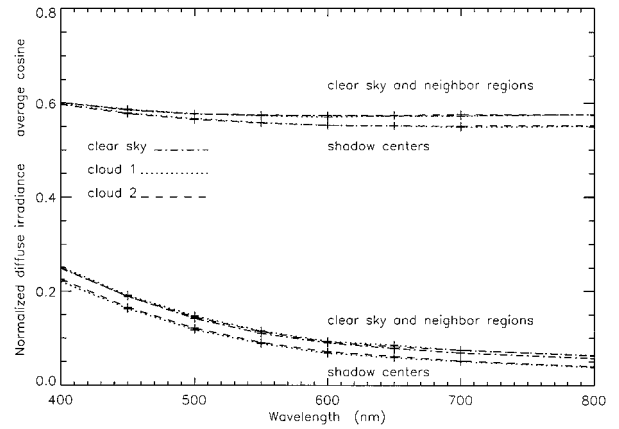 at the shadow centers varies from the clear sky values by less than 10% in the worst case. The normalized downward diffuse irradiance at the neighbor points is also indistinguishable from the clear sky value. The normalized downward diffuse irradiance at the shadow centers differs between cloud 1 and cloud 2 because of differences in cloud sizes and heights.

Elterman's standard atmosphere represents conditions that are much more turbid than those prevailing when the image of Fig. 4 was acquired. Accurate modeling of these very clear conditions required scaling of Elterman's aerosol profile so that $\tau_a(550 \text{ nm}) = 0.0375$. The simulations for Fig. 10 were repeated using the scaled atmosphere, and the results are shown in Fig. 11. Note that for the clear conditions, the difference in diffuse irradiance at the center of the shadows for the two clouds is negligible and that the difference in diffuse irradiance between the shadow and neighbor regions is much less than for the turbid conditions shown in Fig. 10.

Geometric arguments dictate that if the average cosines for downward diffuse irradiance were the same in the shadow and neighbor regions, then the remote-sensing reflectances for downward diffuse irradiance in the two regions would also be equal. Figures 10 and 11 show that the average cosines are not equal, but vary by less than 10%. For the present, assume that the small differences in downward average cosines can be neglected. Then

$$_{\text{sky}}R_{\text{rs(shadow)}} = {}_{\text{sky}}R_{\text{rs(neighbor)}} = R_{\text{rs}}, \qquad (A1)$$

$$_{\Delta\text{sky}}L_{ws} = R_{\text{rs}}[{}_{\text{sky}}E_d(0^+)_{\text{(neighbor)}}$$
$$- E_d(0^+)_{\text{(shadow)}}]. \qquad (A2)$$

The consequences of miscalculating $_{\Delta\text{sky}}L_{ws}$ can be understood qualitatively by examining its importance in Eq. (14) with respect to the term $({}_{\text{sol}}L_{wn} + {}_{\Delta\text{sky}}L_{ws})$. Again, assuming that Eq. (A1) holds,

$$_{\Delta\text{sky}}L_{ws}/({}_{\text{sol}}L_{wn} + {}_{\Delta\text{sky}}L_{ws}) = [{}_{\text{sky}}E_d(0^+)_{\text{(neighbor)}}$$
$$- E_d(0^+)_{\text{(shadow)}}]/[{}_{\text{sol}}E_d(0^+)_{\text{(neighbor)}} + {}_{\text{sky}}E_d(0^+)_{\text{(neighbor)}}$$
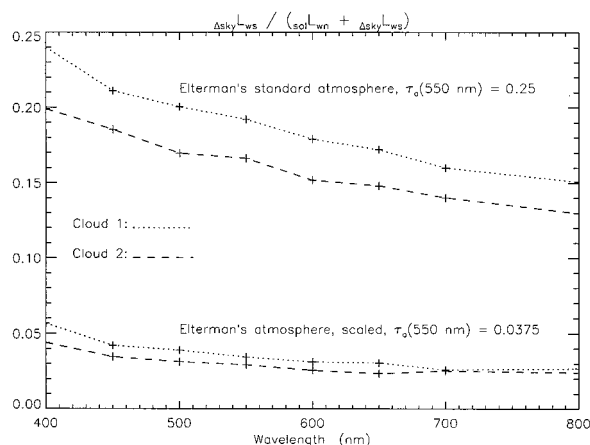$$- E_d(0^+)_{\text{(shadow)}}]. \qquad (A3)$$

Fig. 12. Values of the right-hand side of Eq. (A3) for cloud 1 and cloud 2 embedded in Elterman's standard and scaled atmospheres.

The values of the right-hand side of Eq. (A3) are shown in Fig. 12 for cloud 1 and cloud 2, each embedded in both Elterman's standard and scaled atmosphere. Note that omission of $_{\Delta sky}L_{ws}$ can lead to an error as high as 25% in the calculation of $_{sol}L_{wn}$, and hence in R_{rs}, when modeling clouds approximately the size and height used in this demonstration if they are embedded in a very turbid atmosphere. However, accurate estimation of $_{\Delta sky}L_{ws}$ becomes less important when the cloud-shadow method is used in very clear conditions where it contributes less than 3% in the calculation of $R_{rs}(700\ nm)$.

References

1. H. R. Gordon and D. K. Clark, "Clear water radiances for atmospheric correction of coastal zone color scanner imagery," Appl. Opt. **20,** 4175–4180 (1981).
2. H. R. Gordon, "Calibration requirements and methodology for remote sensors viewing the oceans in the visible," Remote Sensing Environ. **22,** 103–126 (1987).
3. W. A. Hovis, J. S. Knoll, and G. R. Smith, "Aircraft measurements for calibration of an orbiting spacecraft sensor," Appl. Opt. **24,** 407–410 (1985).
4. H. R. Gordon and A. Y. Morel, *Remote Assessment of Ocean Color for Interpretation of Satellite Visible Imagery: A Review* (Springer-Verlag, New York, 1983).
5. K. L. Carder, P. Reinersman, R. G. Steward, R. F. Chen, F. Muller-Karger, C. O. Davis, and M. Hamilton, "AVIRIS calibration and application in coastal oceanic environments," Remote Sensing Environ. **44,** 205–216 (1993).
6. R. O. Green, T. G. Chrien, P. J. Nielson, C. M. Sarture, B. T. Eng, C. Chovit, A. T. Murray, M. L. Eastwood, and H. I. Novack, "Airborne visible/infrared imaging spectrometer (AVIRIS): recent improvements to the sensor and data facility," in *Imaging Spectrometry of the Terrestrial Environment*, G. Vane, ed., Proc. SPIE **1937,** 180–190 (1993).
7. H. Gordon, D. Clark, J. Brown, O. Brown, R. Evans, and W. Broenkow, "Phytoplankton pigment concentrations in the Middle Atlantic Bight: comparison of ship determinations and CZCS estimates," Appl. Opt. **22,** 20–36 (1983).
8. H. R. Gordon, D. K. Clark, J. W. Brown, O. B. Brown, R. H. Evans, and W. W. Broenkow, "Phytoplankton pigment concentrations in the Middle Atlantic Bight: comparison of ship determinations and CZCS estimates," Appl. Opt. **22,** 20–36 (1983).
9. D. Tanre, M. Herman, and P. Dechamps, "Influence of the background contribution upon space measurements of ground reflectance," Appl. Opt. **20,** 3676–3684 (1981).
10. F. Kneizys, E. Shettle, L. Abreu, J. Chetwynd, G. Anderson, W. Gallery, J. Selby, and S. Clough, "User's guide to LOWTRAN-7," Rep. AFGL-TR-88-0177 (U.S. Air Force Geophysics Laboratory, Hanscom Air Force Base, Mass., 1988).
11. P. N. Reinersman and K. L. Carder, "Monte Carlo simulation of the atmospheric point-spread function with an application to correction for the adjacency effect," Appl. Opt. **34,** 4453–4471 (1995).
12. L. Elterman, "UV, visible, and IR attenuation for altitudes to 50 km," Rep. AFCRL-68-0153 (U.S. Air Force Cambridge Research Laboratory, Bedford, Mass., 1968).
13. W. Gregg and K. Carder, "A simple spectral solar irradiance model for cloudless maritime atmosphere," Limnol. Oceanogr. **35,** 1657–1675 (1990).
14. S. Sathyendranath and T. Platt, "The spectral irradiance field at the surface and in the interior of the ocean: a model for applications in oceanography and remote sensing," J. Geophys. Res. **93,** 9270–9280 (1988).
15. H. Neckel and D. Labs, "The solar radiation between 3300 and 12500 A.," Sol. Phys. **90,** 205–258 (1984).
16. C. Cox and W. Munk, "Measurements of the roughness of the sea surface from photographs of the sun's glitter," J. Opt. Soc. Am. **44,** 838–850 (1954).
17. C. Mobley, B. Gentili, H. R. Gordon, Z. Jin, G. W. Kattawar, A. Morel, T. G. Floppini, K. Stamnes, and R. H. Stavn, "Comparison of numerical models for computing underwater light fields," Appl. Opt. **32,** 7484–7504 (1993).
18. H. R. Gordon, "Ship perturbation of irradiance measurements at sea. 1: Monte Carlo simulations," Appl. Opt. **24,** 4172–4182 (1985).
19. J. Li, D. J. W. Geldart, and P. Chylek, "Solar radiative transfer in clouds with vertical internal inhomogeneity," J. Atmos. Sci. **51,** 2542–2552 (1994).
20. H. W. Barker, "Solar radiative transfer for wind-sheared cumulus cloud fields," J. Atmos. Sci. **51,** 1141–1156 (1994).